Electronic Supplementary Information

Parametric Study of Methyl Orange Removal Using Metal–Organic Frameworks Based on Factorial Experimental Design Analysis

Abdollah Karami [1,2], Reem Shomal [1], Rana Sabouni [1,*], Mohammad H. Al-Sayah [3] and Ahmed Aidan [1]

[1] Department of Chemical Engineering, American University of Sharjah, Sharjah P.O. Box 26666, United Arab Emirates; b00029371@alumni.aus.ed (A.K.); rshomal@aus.edu (R.S.); aidan@aus.edu (A.A.)
[2] Department of Chemical Engineering, McMaster University, Hamilton, ON L8S 4L8, Canada
[3] Department of Chemistry, Biology and Environmental Sciences, American University of Sharjah, Sharjah P.O. Box 26666, United Arab Emirates; malsayah@aus.edu
* Correspondence: rsabouni@aus.edu

S1. Adsorption Kinetics

Kinetic experiments were carried out at different initial concentrations (5 –15 mg/L). The kinetic data obtained were analyzed using pseudo-first-order (PFO) [86], pseudo-second-order (PSO) [87] and Elovich [88] models. The PFO, PSO and Elovich kinetic models are given in equations (S1), (S2) and (S3), respectively,

$$q_t = q_e\left(1 - e^{-k_1 t}\right) \tag{S1}$$

$$q_t = \frac{k_2 q_e^2 t}{1 + k_2 q_e t} \tag{S2}$$

$$q_t = \frac{1}{\beta} ln\left(1 + \alpha\beta t\right) \tag{S3}$$

where k_1 (min^{-1}) represents the PFO kinetic constant, k_2 ($g.mg^{-1}.min^{-1}$) is the PSO kinetic constant, α ($mg.g^{-1}.min^{-1}$) is the initial adsorption rate and β ($g.mg^{-1}$) is the desorption constant related to the extent of surface coverage and the activation energy. All kinetic parameters were determined using non-linear regression technique.

The determined kinetic models' parameters along with their corresponding R^2, *RMSE*, and *SSE* are summarized in Table S1. The results shown in Figure S1 reveal that the Elovich model provides the best fit for the experimental data in the case of MO adsorption over Fe-BTC, while for ZIF-8, both PFO and PSO provided a good fit for the experimental data, with the PSO being slightly superior. Also, in the case of Fe-BTC, the calculated q_e values (Table S1) from the PSO model show good agreement with the experimental q_e while for ZIF-8, both PFO and PSO provided good agreement between $q_{e,exp,}$ and $q_{e,calc}$. Regarding the PSO rate constant (k_2), the results showed that the rate constant decreases with increasing

initial MO concentration in the case of Fe-BTC. This can be ascribed to increasing competition for active adsorption sites as initial concentration increases [89–91]. In contrast, for ZIF-8, the rate constant increased with increasing initial MO concentration indicating the faster adsorption rate due to enhanced interaction between MO and ZIF-8 (i.e., higher driving force for mass transfer) [92–94]. Further, the rate constant values for Fe-BTC were greater than those for ZIF-8, confirming the higher removal efficiency results. Finally, the high R^2 values and the low *RMSE and SSE* values obtained for the Elovich model indicate that the adsorption of MO on Fe-BTC might be heterogeneous (i.e., the adsorbing surface is heterogeneous) [95,96].

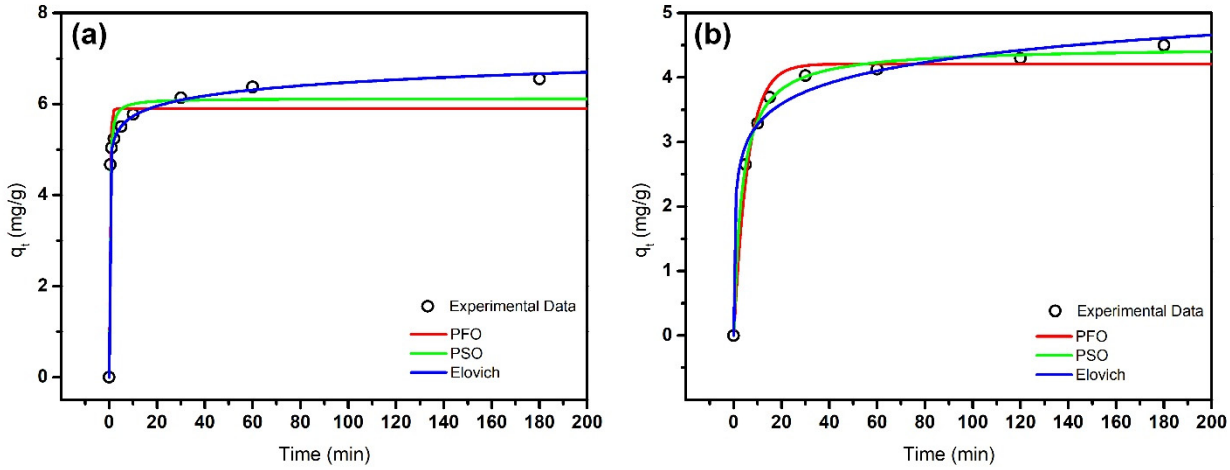

Figure S1. Kinetic models fitted to the experimental data (m = 100 mg, C_o = 15 mg/L) for (a) Fe-BTC, (b) ZIF-8

Table S1. Summary of kinetic parameters for MO adsorption over Fe-BTC and ZIF-8.

MOF	Kinetic Model	Parameters	C_o (mg/L)		
			5	10	15
		$q_{e,exp}$ (mg.g^{-1})	2.029	4.262	6.550
Fe-BTC	PFO	k_1 (min^{-1})	2.425	2.924	2.726
		$q_{e,calc}$ (mg.g^{-1})	1.847	3.866	5.896
		R^2	0.943	0.954	0.950
		RMSE	0.160	0.299	0.476
		SSE	0.179	0.626	1.585
	PSO	k_2 (g.mg^{-1}.min^{-1})	2.265	1.405	0.838
		$q_{e,calc}$ (mg.g^{-1})	1.922	4.007	6.118
		R^2	0.979	0.981	0.979
		RMSE	0.097	0.191	0.308
		SSE	0.065	0.256	0.663

	Elovich	α **(mg.g^{-1}.min^{-1})**	1.438×10^{5}	4.302×10^{6}	1.765×10^{6}
		β **(g.mg^{-1})**	9.194	5.089	3.108
		R^2	0.995	0.998	0.999
		RMSE	0.046	0.059	0.069
		SSE	0.015	0.025	0.033
ZIF-8		$q_{e,exp}$ **(mg.g^{-1})**	2.040	3.691	4.500
	PFO	k_1 **(min^{-1})**	0.061	0.093	0.170
		$q_{e,calc}$ **(mg.g^{-1})**	2.004	3.423	4.208
		R^2	0.996	0.984	0.984
		RMSE	0.060	0.191	0.199
		SSE	0.018	0.145	0.238
	PSO	k_2 **(g.mg^{-1}.min^{-1})**	0.034	0.046	0.065
		$q_{e,calc}$ **(mg.g^{-1})**	2.257	3.665	4.475
		R^2	0.989	0.996	0.998
		RMSE	0.095	0.098	0.070
		SSE	0.045	0.038	0.030
	Elovich	α **(mg.g^{-1}.min^{-1})**	0.394	31.920	53.670
		β **(g.mg^{-1})**	2.292	2.637	2.157
		R^2	0.953	0.999	0.984
		RMSE	0.191	0.054	0.198
		SSE	0.182	0.012	0.236

To further understand the diffusion mechanism involved in MO adsorption over Fe-BTC and ZIF-8, the intraparticle diffusion kinetics were investigated using the Weber-Morris intraparticle diffusion (IPD) model [97], which is expressed in equation (S4),

$$q_t = k_p t^{0.5} + C \quad \text{(S4)}$$

where k_P (mg.g^{-1}.min$^{-0.5}$) is the intraparticle diffusion rate constant and C (mg.g^{-1}) is the intraparticle diffusion constant related to the thickness of boundary layer [97]. Based on the IPD model, the plot of q_t versus $t^{0.5}$ should yield a straight line passing through the origin if intraparticle diffusion was the only rate-limiting step in the adsorption process [98]. Multi-linearity, on the other hand, is indicative of multiple mechanisms that control the adsorption process [99]. As shown in Figure S2, the obtained data for both Fe-BTC and ZIF-8 at different initial concentrations were not linear over the entire time range. Instead, they exhibited a tri-linear behavior, suggesting the existence of three successive adsorption

stages. This multi-linear behavior has been reported in previous investigations [69,100]. Each linear segment represents a controlling mechanism. In the first step, external surface adsorption related to diffusion through the boundary layer. In the second step, IPD takes place. The third step is the equilibrium stage, where adsorption slows as surface coverage approaches saturation.

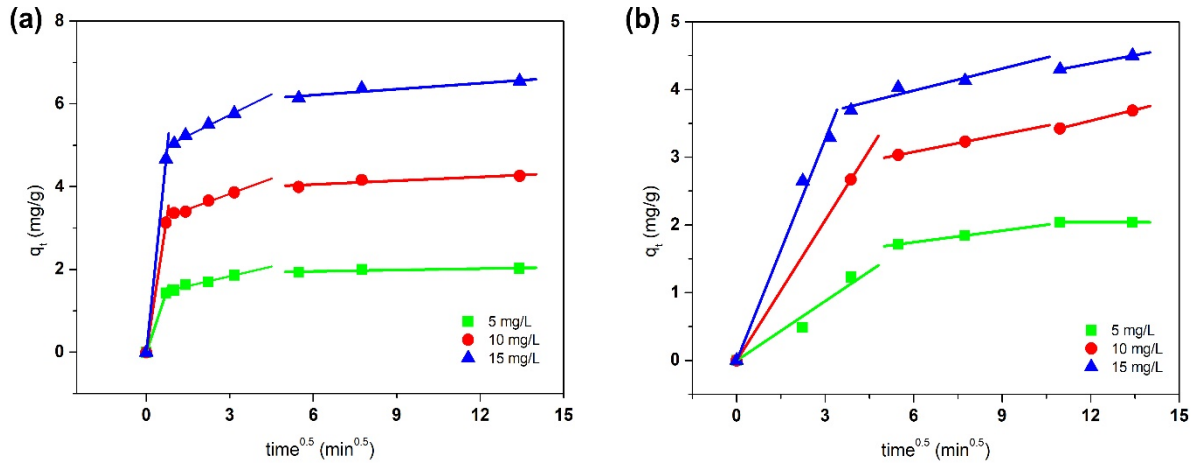

Figure S2. Intraparticle diffusion model plot of MO adsorption over (a) Fe-BTC and (b) ZIF-8 (m = 100 mg)

S2. Adsorption Isotherms

Equilibrium adsorption isotherms of MO were studied with initial concentration ranges of 10–250 mg/L and MOF dosage of 50 mg. The obtained adsorption equilibrium data were fitted to Langmuir [101], Freundlich [102], Dubinin-Radushkevich (D-R) [102], and Temkin[102] isotherm models. The Langmuir isotherm model is given in equation (S5).

$$q_e = \frac{q_m K_L C_e}{1 + K_L C_e} \tag{S5}$$

where q_m is the maximum monolayer adsorption capacity (mg/g) with the highest dye concentration used in the experiment, K_L is the Langmuir constant (L/mg) associated with the adsorption rate. From the K_L value calculated from the Langmuir model, the Langmuir dimensionless separation factor or equilibrium parameter (R_L) is calculated by Equation (S6).

$$R_L = \frac{1}{(1 + K_L C_o)} \tag{S6}$$

where R_L indicate the shape of the isotherm to be either irreversible (R_L=0), favorable (0<R_L<1), linear (R_L=1), or unfavorable (R_L>1).

Equation (S7) describes the Freundlich isotherm model.

$$q_e = K_F C_e^{1/n} \tag{S7}$$

where n and K_f ((mg.g^{-1})(Lmg^{-1})$^{1/n}$) are Freundlich constants related to the favorability of the adsorption process and the adsorption capacity of the adsorbate, respectively. If ($1/n$)<1, it indicates favorable adsorption.

Also, the Temkin isotherm is given in Equation (S8)

$$q_e = \frac{RT}{b_T} ln(K_T C_e) \tag{S8}$$

where K_T (L.mg^{-1}) is the Temkin isotherm constant, and b_T (kJ.mol^{-1}) is the constant related to the heat of adsorption. R is the universal gas constant, and T (K) is the absolute temperature.

Finally, equations (S9) and (S10) present the D-R isotherm model.

$$q_e = q_{DR} e^{-K_{DR}\varepsilon^2} \tag{S9}$$

$$\varepsilon = RT\, ln\left(1 + \frac{1}{C_e}\right) \tag{S10}$$

where q_{DR} (mg.g^{-1}) is the D-R constant representing the theoretical adsorption capacity, ε is the Polanyi potential, and K_{DR} (mol^2.kJ^{-2}) is the constant of the adsorption energy which can be correlated to the mean adsorption energy (E) by using equation (S11).

$$E = \frac{1}{\sqrt{2K_{DR}}} \tag{S11}$$

In general, the calculated value of E can give an insight into whether the adsorption is a physical or chemical process. If the value of E is between 8 and 16 kJ.mol^{-1}, then the adsorption is dominated by a chemical mechanism, while if E is less than 8 kJ.mol^{-1}, then the adsorption proceeds through a physical mechanism [104-108].

Figure S3 represents the non-linear plots of the four isotherm models fitted to the experimental data of q_e versus C_e at 298 K for both Fe-BTC and ZIF-8. The calculated maximum adsorption capacities, isotherm parameters and the respective values of R^2, *RMSE*, and *SSE* are summarized in Table S2. Among the four models, Langmuir had the best fitting parameters (highest R^2 and lowest *RMSE* and *SSE*) for both MOFs. It can be noticed that the calculated q_m increases as temperature increases in the case of MO adsorption over Fe-BTC, whereas the opposite is noticed in the case of ZIF-8. This suggests that the adsorption is more effective at a higher temperature for Fe-BTC in contrast to the ZIF-8, where adsorption is favored at a lower temperature. Also, the Langmuir separation factor (R_L) as a function of initial concentration at 298, 303 and 313 K is shown in Figure S4. All the values were between 0 and 1 indicating that the adsorption process is favorable for both Fe-BTC and ZIF-8. However, in the case of Fe-BTC, the values of R_L at higher temperatures were smaller than those at lower temperatures, while the opposite was true for ZIF-8, hence, confirming the conclusions from the calculated q_m at different temperatures. In addition, all of the n values in the Freundlich isotherm were greater than unity which

means (1/n)<1, hence, the adsorption of MO on Fe-BTC and ZIF-8 is favorable. Finally, the values of the mean adsorption energy (*E*) calculated from the D-R isotherm (Table S2) in both cases suggest that the adsorption of MO proceeds through physical adsorption.

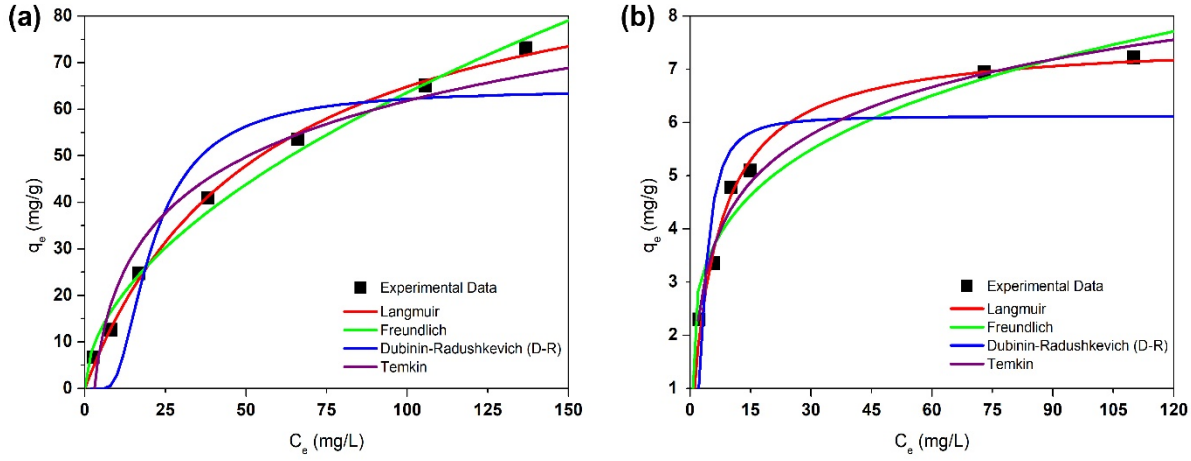

Figure S3. Equilibrium adsorption isotherms of MO adsorption on (a) Fe-BTC and (b) ZIF-8 at 298 K

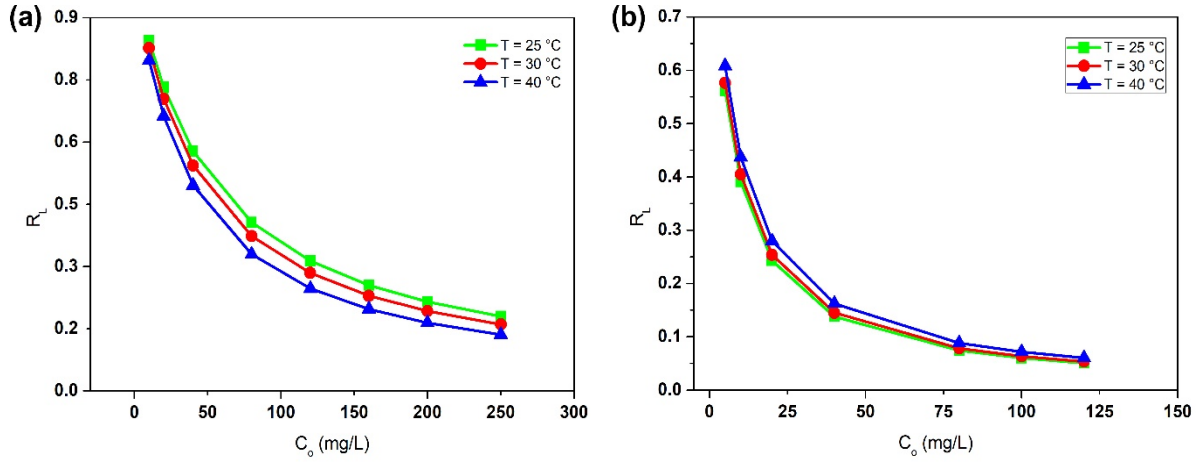

Figure S4. Plot of the Langmuir dimensionless separation factor (R_L) vs. C_o at different temperatures for (a) Fe-BTC and (b) ZIF-8

Table S2. Summary of adsorption isotherms for MO adsorption on Fe-BTC and ZIF-8.

MOF	**Isotherm Model**	**Parameters**	***T* (K)**		
			298	**303**	**313**
Fe-BTC	**Langmuir**	q_m **(mg/g)**	100.3	105.0	114.0
		K_L **(L/mg)**	0.018	0.021	0.025
		R^2	0.997	0.998	0.991
		RMSE	1.508	1.967	4.020
		SSE	11.370	11.610	48.470
	Freundlich	K_F **(mg.g^{-1})(L.mg^{-1})$^{1/n}$**	5.375	6.103	7.423

		n	1.864	1.948	1.917
		R^2	0.990	0.991	0.967
		RMSE	2.867	4.088	7.808
		SSE	41.090	50.140	182.900
	Temkin	K_T **(L.mg^{-1})**	0.350	0.449	0.502
		b_T **(kJ.mol^{-1})**	0.143	0.135	0.128
		R^2	0.951	0.987	0.967
		RMSE	6.264	4.960	7.729
		SSE	196.2	73.8	179.2
	Dubinin-Radushkevich (D-R)	K_{DR} **(mol^2.kJ^{-2})**	54.99	13.62	11.78
		q_{DR} **(mg.g^{-1})**	64.30	77.56	78.07
		E **(kJ.mol^{-1})**	0.095	0.192	0.206
		R^2	0.886	0.969	0.951
		RMSE	9.534	7.554	9.499
		SSE	454.5	171.2	270.7
ZIF-8	**Langmuir**	q_m **(mg/g)**	7.56	5.62	4.65
		K_L **(L/mg)**	0.156	0.147	0.129
		R^2	0.987	0.988	0.997
		RMSE	0.249	0.133	0.067
		SSE	0.248	0.053	0.009
	Freundlich	K_F **(mg.g^{-1})(L.mg^{-1})$^{1/n}$**	2.385	1.946	1.570
		n	4.080	4.302	4.470
		R^2	0.939	0.934	0.956
		RMSE	0.535	0.305	0.251
		SSE	1.143	0.280	0.126
	Temkin	K_T **(L.mg^{-1})**	2.940	3.012	2.860
		b_T **(kJ.mol^{-1})**	1.923	2.586	3.345
		R^2	0.980	0.960	0.983
		RMSE	0.308	0.239	0.155
		SSE	0.381	0.172	0.048
	Dubinin-Radushkevich (D-R)	K_{DR} **(mol^2.kJ^{-2})**	2.01	5.35	5.87
		q_{DR} **(mg.g^{-1})**	6.119	4.898	4.089
		E **(kJ.mol^{-1})**	0.499	0.306	0.292

		R^2	0.700	0.898	0.909
		RMSE	1.188	0.379	0.363
		SSE	5.642	0.431	0.263

S3. Adsorption Thermodynamics

To understand the effect of temperature on the adsorption capacity and removal efficiency, the adsorption of MO at various temperatures (298, 303, and 313 K) was investigated and the thermodynamic parameters such as Gibbs free energy (ΔG°), change in enthalpy (ΔH°), and change in entropy (ΔS°) were calculated. These parameters provide an insight into the mechanism related to the adsorption process being investigated. ΔG°, ΔH°, and ΔS° are calculated using equations (S12) and (S13),

$$\Delta G^o = -RT\,ln\left(K_{eq}\right) \tag{S12}$$

$$ln\left(K_{eq}\right) = \frac{\Delta S^o}{R} - \frac{\Delta H^o}{RT} \tag{S13}$$

where K_{eq} is the adsorption equilibrium constant. The Van't Hoff plot of equation (S13) relates the change in adsorption equilibrium constant, K_{eq}, to the change in temperature, and is used to estimate ΔH° and ΔS° of the adsorption process. In order to obtain meaningful values for the thermodynamic parameters, the value of K_{eq} has to be estimated properly. Since the Langmuir isotherm model was the best among the four models used in fitting the experimental data, the Langmuir constant (K_L) was used to estimate the equilibrium constant (K_{eq}) using the method suggested by Zhou and Zhou [106].

The results of the thermodynamic calculations are listed in Table S3, and the Van't Hoff plot used to estimate ΔH°, and ΔS° of MO adsorption on Fe-BTC and ZIF-8 is presented in Figure S5. The negative ΔG° values for both Fe-BTC and ZIF-8 reflects the spontaneous nature of the adsorption process under the experimental conditions. For Fe-BTC, the positive ΔH° value (16.86 kJ.mol^{-1}), confirms the endothermic adsorption of MO over Fe-BTC. This behavior may be attributed to the enhanced mobility of MO molecules from the bulk solution towards the Fe-BTC surface with increasing temperature. Also, at a higher temperature, MO molecules may gain more energy to interact with the active sites at the adsorbent's surface [77]. The endothermic adsorption of MO and other dyes using MOFs have been reported in the literature [109]–[111]. In contrast, the negative ΔH° (-9.94 kJ.mol^{-1}) for ZIF-8 confirms the exothermic MO adsorption. The calculated absolute values of ΔH° are less than 40 kJ.mol^{-1}, which indicates that MO adsorption over Fe-BTC and ZIF-8 proceeds in a physical adsorption mechanism [69], [73]. This was also confirmed by the results of the D-R isotherm model. In addition, the positive values of ΔS° (162.4 and 90.2 J.mol^{-1}.K^{-1} for Fe-BTC and ZIF-8, respectively) reflects the increased disorder of the system at the solid-solution interface. This is due to the increased mobility of water

molecules when the solvated MO molecules move from the bulk solution to the surface of the adsorbent. Also, in the case of Fe-BTC, the number of pre-adsorbed water molecules released from the surface of the adsorbent is more than the number of MO molecules adsorbed (i.e., the adsorption of a single MO molecule desorbs several water molecules due to larger MO molecule size compared to water), hence, $\Delta S°$ for Fe-BTC is larger than ZIF-8. This reveals that entropy change is a major driving force of MO adsorption on Fe-BTC.

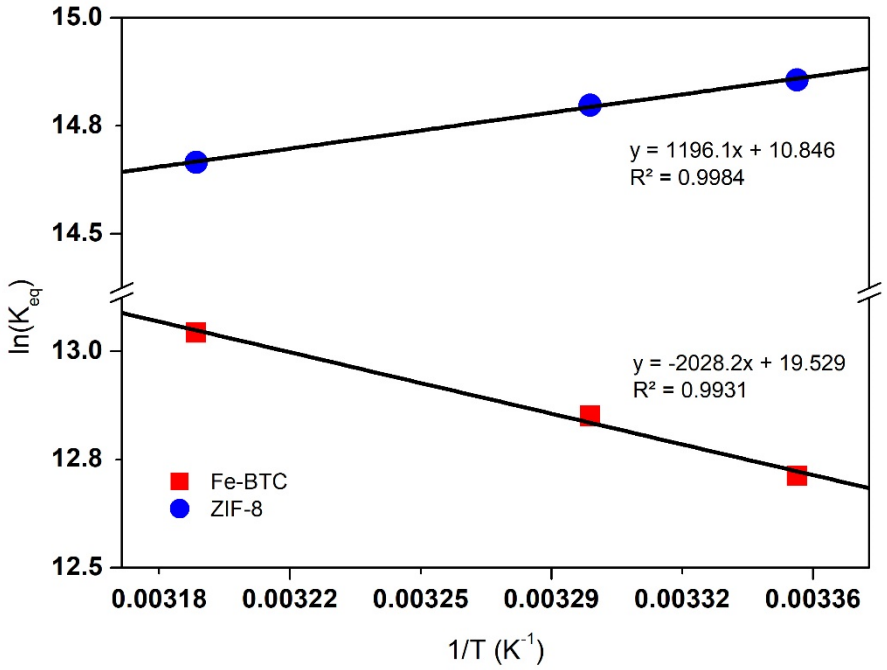

Figure S5: Van't Hoff plot to obtain ΔH° and ΔS° of MO adsorption on Fe-BTC and ZIF-8

Table S3: Thermodynamic parameters of MO adsorption over Fe-BTC and ZIF-8.

MOF	T (K)	ΔG° (kJ.mol^{-1})	ΔH° (kJ.mol^{-1})	ΔS° (J.mol^{-1}.K^{-1})	R^2
Fe-BTC	298	-31.50	16.86	162.4	0.9931
	303	-32.37			
	313	-33.94			
ZIF-8	298	-36.81	-9.94	90.2	0.9984
	303	-37.28			
	313	-38.16			

S4. Desorption and Regeneration Study

From a commercial standpoint, regeneration and reusability of an adsorbent are crucial aspects to be considered. In this work, a simple method of washing with ethanol was utilized to regenerate MO-loaded MOFs. After MO adsorption (C_o is 15 mg/L and m is 200 mg), Fe-BTC was separated from the

solution by centrifugation (6000 rpm for 30 min), while ZIF-8 was separated using vacuum filtration. Then, the MO-loaded MOFs were washed by mixing with ethanol on a magnetic stirrer at room temperature for at least 1 hour. The washing and solid/liquid separation steps were repeated several times. Finally, the recovered MOFs were dried under a vacuum at 100 °C and then reused for a second adsorption experiment. The results showed that both Fe-BTC and ZIF-8 could be regenerated easily using ethanol. For Fe-BTC the decrease in the removal efficiency was 12% (99% to 87%) compared to 16% (61% to 51%) for ZIF-8. However, in the case of Cu-BTC, regeneration attempts were unfruitful.

References

86. Tan, K.L.; Hameed, B.H. Insight into the adsorption kinetics models for the removal of contaminants from aqueous solutions. *J. Taiwan Inst. Chem. Eng.* **2017**, *74*, 25–48. https://doi.org/10.1016/j.jtice.2017.01.024.
87. Ho, Y.S.; McKay, G. Pseudo-second order model for sorption processes. *Process Biochem.* **1999**, *34*, 451–465. https://doi.org/10.1016/S0032-9592(98)00112-5.
88. Ghaedi, M.; Ghaedi, A.M.; Negintaji, E.; Ansari, A.; Vafaei, A.; Rajabi, M. Random forest model for removal of bromophenol blue using activated carbon obtained from Astragalus bisulcatus tree. *J. Ind. Eng. Chem.* **2014**, *20*, 1793–1803. https://doi.org/10.1016/j.jiec.2013.08.033.
89. Tong, M.; Liu, D.; Yang, Q.; Devautour-Vinot, S.; Maurin, G.; Zhong, C. Influence of framework metal ions on the dye capture behavior of MIL-100 (Fe, Cr) MOF type solids. *J. Mater. Chem. A* **2013**, *1*, 8534. https://doi.org/10.1039/c3ta11807j.
90. Ji, W.-J.; Hao, R.-Q.; Pei, W.-W.; Feng, L.; Zhai, Q.-G. Design of two isoreticular CD-biphenyltetracarboxylate frameworks for Dye adsorption, separation and photocatalytic degradation. *Dalton Trans.* **2018**, *47*, 700–707.
91. Hameed, B.H.; Rahman, A.A. Removal of phenol from aqueous solutions by adsorption onto activated carbon prepared from biomass material. *J. Hazard. Mater.* **2008**, *160*, 576–581. https://doi.org/10.1016/j.jhazmat.2008.03.028.
92. Din, A.T.M.; Hameed, B.H.; Ahmad, A.L. Batch adsorption of phenol onto physiochemical-activated coconut shell. *J. Hazard. Mater.* **2009**, *161*, 1522–1529. https://doi.org/10.1016/j.jhazmat.2008.05.009.
93. Srivastava, V.C.; Swamy, M.M.; Mall, I.D.; Prasad, B.; Mishra, I.M. Adsorptive removal of phenol by bagasse fly ash and activated carbon: Equilibrium, kinetics and thermodynamics. *Colloids Surfaces A Physicochem. Eng. Asp.* **2006**, *272*, 89–104. https://doi.org/10.1016/j.colsurfa.2005.07.016.
94. Teng, H.; Hsieh, C.-T. Activation Energy for Oxygen Chemisorption on Carbon at Low Temperatures. *Ind. Eng. Chem. Res.* **1999**, *38*, 292–297. https://doi.org/10.1021/ie980107j.
95. Piasecki, W.; Rudziński, W. Application of the statistical rate theory of interfacial transport to investigate the kinetics of divalent metal ion adsorption onto the energetically heterogeneous surfaces of oxides and activated carbons. *Appl. Surf. Sci.* **2007**, *253*, 5814–5817. https://doi.org/10.1016/j.apsusc.2006.12.066.
96. Weber, W.J.; Morris, J.C. Kinetics of Adsorption on Carbon from Solution. *J. Sanit. Eng. Div.* **1963**, *89*, 31–60.
97. Mittal, A.; Malviya, A.; Kaur, D.; Mittal, J.; Kurup, L. Studies on the adsorption kinetics and isotherms for the removal and recovery of Methyl Orange from wastewaters using waste materials.. *J. Hazard. Mater.* **2007**, *148*, 229–240,. https://doi.org/10.1016/j.jhazmat.2007.02.028.
98. Wu, F.C.; Tseng, R.L.; Juang, R.S. Initial behavior of intraparticle diffusion model used in the description of adsorption kinetics. *Chem. Eng. J.* 2009. https://doi.org/10.1016/j.cej.2009.04.042.
99. Machado, F.M.; Bergmann, C.P.; Lima, E.C.; Royer, B.; de Souza, F.E.; Jauris, I.M.; Calvete, T.; Fagan, S.B. Adsorption of Reactive Blue 4 dye from water solutions by carbon nanotubes: Experiment and theory. *Phys. Chem. Chem. Phys.* **2012**, *14*, 11139. https://doi.org/10.1039/c2cp41475a.
100. Dhakshinamoorthy, A.; Alvaro, M.; Garcia, H. Aerobic oxidation of cycloalkenes catalyzed by iron metal organic framework containing N-hydroxyphthalimide. *J. Catal.* **2012**, *289*, 259–265. https://doi.org/10.1016/j.jcat.2012.02.015.
101. Langmuir, I. The adsorption of gases on plane surfaces of glass, mica and platinum. *J. Am. Chem. Soc.* **1918**, *40*, 1361–1403. https://doi.org/10.1021/ja02242a004.
102. Liu, Y.; Liu, Y.-J. Biosorption isotherms, kinetics and thermodynamics. *Sep. Purif. Technol.* **2008**, *61*, 229–242. https://doi.org/10.1016/j.seppur.2007.10.002.
103. Kousha, M.; Daneshvar, E.; Sohrabi, M.S.; Jokar, M.; Bhatnagar, A. Adsorption of acid orange II dye by raw and chemically modified brown macroalga Stoechospermum marginatum. *Chem. Eng. J.* **2012**, *192*, 67–76. https://doi.org/10.1016/j.cej.2012.03.057.

104. Vijayaraghavan, K.; Padmesh, T.; Palanivelu, K.; Velan, M. Biosorption of nickel(II) ions onto Sargassum wightii: Application of two-parameter and three-parameter isotherm models. *J. Hazard. Mater.* **2006**, *133*, 304–308. https://doi.org/10.1016/j.jhazmat.2005.10.016.
105. Basar, C. Applicability of the various adsorption models of three dyes adsorption onto activated carbon prepared waste apricot. *J. Hazard. Mater.* **2006**, *135*, 232–241. https://doi.org/10.1016/j.jhazmat.2005.11.055.
106. Zhou, X.; Zhou, X. The unit problem in the thermodynamic calculation of adsorption using the Langmuir equation. *Chem. Eng. Commun.* **2014**, *201*, 1459–1467. https://doi.org/10.1080/00986445.2013.818541.
107. Mahmoodi, N.M.; Najafi, F. Synthesis, amine functionalization and dye removal ability of titania/silica nano-hybrid. *Microporous Mesoporous Mater.* **2012**, *156*, 153–160. https://doi.org/10.1016/j.micromeso.2012.02.026.
108. Shen, T.; Luo, J.; Zhang, S.; Luo, X. Hierarchically mesostructured MIL-101 metal–organic frameworks with different mineralizing agents for adsorptive removal of methyl orange and methylene blue from aqueous solution. *J. Environ. Chem. Eng.* **2015**, *3*, 1372–1383. https://doi.org/10.1016/j.jece.2014.12.006.
109. Haque, E.; Lo, V.; Minett, A.I.; Harris, A.T.; Church, T.L. Dichotomous adsorption behaviour of dyes on an amino-functionalised metal–organic framework, amino-MIL-101(Al). *J. Mater. Chem. A* **2014**, *2*, 193–203,. https://doi.org/10.1039/C3TA13589F.
110. Angin, D. Utilization of activated carbon produced from fruit juice industry solid waste for the adsorption of Yellow 18 from aqueous solutions.. *Bioresour. Technol.* **2014**, *168*, 259–266, https://doi.org/10.1016/j.biortech.2014.02.100.
111. Kara, M.; Yuzer, H.; Sabah, E.; Celik, M. Adsorption of cobalt from aqueous solutions onto sepiolite. *Water Res.* **2003**, *37*, 224–232, https://doi.org/10.1016/S0043-1354(02)00265-8.